Polymer 49 (2008) 5002–5012

Contents lists available at ScienceDirect

Polymer

journal homepage: www.elsevier.com/locate/polymer

# Composite polypyrrole-containing particles and electrical properties of thin films prepared therefrom

Yan Lu [a], Andrij Pich [b], Hans-Juergen P. Adler [b], Geng Wang [c], David Rais [d,*], Stanislav Nešpůrek [d,e]

[a] Physical Chemistry I, University of Bayreuth, D-95440 Bayreuth, Germany
[b] Institute of Macromolecular Chemistry and Textile Chemistry, Dresden University of Technology, D-01062 Dresden, Germany
[c] Department of Chemistry, Tsinghua University, 100084 Beijing, PR China
[d] Institute of Macromolecular Chemistry, Academy of Sciences of the Czech Republic, v.v.i., 162 06 Prague 6, Czech Republic
[e] Faculty of Chemistry, Brno University of Technology, 612 00 Brno, Czech Republic

ARTICLE INFO

*Article history:*
Received 7 April 2008
Received in revised form 15 August 2008
Accepted 22 August 2008
Available online 18 September 2008

*Keywords:*
Core–shell particles
Polypyrrole
Electrical conductivity

ABSTRACT

Preparation of core–shell particles consisting of polystyrene–poly(ethylene glycol) monomethacrylate (PS–PEGMA) core covered with polypyrrole (PPy) shell is described. The thickness of PPy shell, which strongly influences electrical properties of the films prepared from the particles, can be varied by changing pyrrole load, controlling the overall template surface area in the system and by influencing the pyrrole polymerization kinetics in the presence of different oxidants. The type of anions and PPy loading strongly influence the electrical conductivity. Typical value of the resistivity of thin film consisting of core–shell particles was 34 Ωm (PPy oxidized by $FeCl_3$, shell thickness 3 nm). Current–voltage dependences of low conductivity samples (thin PPy shell layer) are characteristic of contact-limited currents. The conductivity of the particles changes with humidity, which can be utilized in humidity sensors.



## 1. Introduction

During the last decade an interest in conducting polymers strongly increased on both scientific and application level. Particularly, polyaniline (PA), polypyrrole (PPy), poly(phenylenevinylene) (PPV) and polythiophene (PT) were the most frequent candidates because of their stability in air, high electrical conductivity and easy synthesis and polymerization [1,2]. However, the electrically conductive unsubstituted polymers are not well soluble and require quite complicated post-synthetic procedures to be prepared in the form suitable for applications. Good results were obtained with film preparation by electrochemical polymerization, but many limitations occur also here.

Recently, extensive efforts have been directed towards improving the processability of electrically conductive polymers. The main approaches can be divided into three groups: (1) preparation of composites with polymer matrices; (2) preparation of soluble derivatives; (3) preparation of dispersions of insoluble conducting particles. Synthesis of polymer dispersions [3,4] requires the selection of appropriate stabilizers (conventional surfactants [5–8] or water-soluble polymers [9–17]) to limit particle coagulation and to control the morphology and size of the polymer particles [18]. Recently, a successful production of PPy latex particles has been reported by chemical oxidative polymerization of pyrrole in either water or other media in the presence of various stabilizers, like poly(vinylpyrrolidone) (PVP), poly(vinyl alcohol-*co*-vinylacetate) (PVA) [19,20], poly(vinyl methyl ether) (PVME) and poly(styrenesulfonate) (PSS) [17]. The size of the formed spherical PPy particles was in the range of 30–200 nm. Production of conductive nanometer-sized objects is still under intensive research and interest from the viewpoint of applications in molecular electronics and photonics [21].

In the previous papers, we described the synthesis of composite PPy particles in the presence of thermosensitive poly(vinyl methyl ether) (PVME) [22] and poly(*N*-vinylcaprolactam-*co*-2-(acetoacetoxy)ethyl methacrylate) (VCL/AAEM) microgels [23,24], which played the roles of both templates and stabilizers. In these cases PPy nanoparticles have been integrated into the porous microgel structure. The preparation of polymer particles coated with the PPy shell can be realized by using compact polymer spheres as demonstrated by Armes and co-workers [25,26]. In the present paper, polystyrene particles with grafted poly(ethylene glycol) monomethacrylate (PEGMA) brush-like layers have been used as templates for the deposition of PPy shells. The synthesis, which is reported in this paper, is examined in two steps: (1) preparation of monodisperse polystyrene particles with appropriate surface and controlled size; (2) deposition of polypyrrole (model material for conducting polymers) during oxidative polymerization process.

* Corresponding author. Tel.: +420 222511696.
*E-mail address:* david.rais@atlas.cz (D. Rais).

0032-3861/$ – see front matter © 2008 Elsevier Ltd. All rights reserved.
doi:10.1016/j.polymer.2008.08.066

Herein we examine the possibilities of controlling the morphology and thickness of the PPy shell as well as the nature of the anion incorporated into the polypyrrole structure. Even though several synthetic routes were described in literature, physical properties and mainly electrical properties of such particles and their possible applications are less frequently reported. In this paper, we present the electrical characteristics of the core–PPy shell particles. The influence of several oxidants on electrical properties of the particles is discussed and possible applications in the construction of humidity sensors are mentioned.

## 2. Experimental

### 2.1. Material

Styrene (ST) (from Fluka) and pyrrole (Py) were purified by conventional methods and then vacuum-distilled under nitrogen. Poly(ethylene glycol) monomethacrylate (PEGMA, Aldrich) with average $M_w = 526\ g\ mol^{-1}$ was used as supplied. Oxidants, sodium peroxydisulfate ($Na_2S_2O_8$), iron(III) chloride ($FeCl_3$), and phosphomolybdic acid ($H_3PMo_{12}O_{40}\cdot 29H_2O$) from Aldrich were used as-received. Distilled water was used as polymerization medium.

#### 2.1.1. Synthesis of PS–PEGMA core particles

Basic information concerning the synthesis of PS–PEGMA particles was reported elsewhere [27]. Here we add some details of the preparation. An appropriate amount of PEGMA was dissolved in water and then styrene was added to the stirred solution. The obtained pre-emulsion was stirred for 1 h. The double-walled glass reactor equipped with a stirrer and reflux condenser was purged with nitrogen. The pre-emulsion was placed in the reactor and a water solution of initiator was added under continuous stirring. Temperature was increased to 70 °C to start the polymerization. Latexes were prepared at ca. 10% solid content and purified by dialysis. The diameter of particles ranged from 120 to 300 nm. The particles consisted of compact hydrophobic polystyrene-rich core and hydrophilic PEGMA-rich swollen shell.

#### 2.1.2. Synthesis of core–shell particles

Polypyrrole was deposited onto surface of preformed PS–PEGMA particles by oxidative pyrrole polymerization. A dilute PS–PEGMA dispersion was placed in stirred reactor. An appropriate pyrrole amount was injected with a syringe and the mixture was stirred for 15 min under nitrogen flow at 25 °C. A water solution of oxidant (e.g., $FeCl_3$) was added dropwise to start the pyrrole polymerization. After 5–10 min, the dispersion became coloured (blue or dark red colour appeared) indicating that the pyrrole polymerization started. After 6 h the formed composite particles were removed from the reaction vessel and washed to remove unreacted pyrrole and all by-products.

### 2.2. Particle characterization and analytical methods

For the determination of particle size, a commercial laser light scattering (LLS) spectrometer (ALV/DLS/SLS-5000) equipped with an ALV-5000/EPP multiple digital time correlator and laser goniometer system ALV/CGS-8F S/N 025 was used with a helium–neon laser (Uniphase 1145P, output 22 mW, wavelength 632.8 nm) as the light source. Measurements were carried out at angles $\theta = 30°$–140°. The investigated sample in a 10-mm test tube was immersed in a toluene bath and thermostatted with accuracy ±0.1 °C. Typically, 5 measurements were performed for determination of hydrodynamic radius; the accuracy was ±3%.

Stability measurements were performed with a separation analyzer LUMiFuge 114 (L.U.M. GmbH, Germany). Measurements were made in glass tubes at 3000 rpm. The slope of sedimentation curves was used to calculate the sedimentation velocity and to get information about the stability of the samples.

Scanning electron microscopy (SEM) images were taken with a Gemini microscope (Zeiss, Germany). Samples were prepared in the following manner: dispersions were diluted with deionized water, dropped onto aluminium substrates and dried at room temperature. Pictures were taken at a voltage of 4 kV.

Atomic force microscopy (AFM) measurements were made with a Dimension 3100 (Digital Instruments Inc.) using the tapping mode regime (set-point ratio – 90%; integral gain – 0.2; proportional gain – 2.0; amplitude set-point – 0.7 V; scan rate – 0.901 Hz). Samples were prepared by spin-coating technique (2000 rpm, 10 min) on cleaned glass substrates.

IR spectra were recorded with a Mattson Instruments Research Series 1 FTIR spectrometer. Dried polymer samples were mixed with KBr and pressed to form pellets.

UV spectra were recorded with a Perkin Elmer UV–VIS spectrometer Lambda 45. This device was equipped with RSA-PE-20 accessory which is an optical bench with transfer optics, an integrating sphere and a detector pre-amplification module. Samples were fixed between two quartz plates.

### 2.3. Electrical characterization of thin films of core-shell particles

Two types of samples were used for the measurements: surface-gap samples with Pt electrodes (distance 50 μm) and sandwich ones with indium-tin-oxide (ITO) and vacuum evaporated Al electrodes. Thin films were prepared by spin-coating technique from dispersions of particles in a two-step procedure: 200 rpm for 10 s and then 3000 rpm for 30 s. The deposited films were dried at 0.1 Pa at 50 °C for 5 h.

DC current–voltage ($j$–$V$) characteristics were measured with Keithley 6517A electrometer. Samples were placed in a vacuum chamber ($10^{-3}$ Pa) with temperature adjustment system. Resistivities were measured using four-point-probe method [28]. Sensitivity to humidity was checked in a homemade apparatus; the relative humidity (RH) was changed from 2 to 98% using a mixture of dry and water saturated nitrogen. RH values were calibrated using a commercial sensor (Testo AG 635-1, Germany). Electrical AC signals were measured with a Hioki 3532-50 LCR Hi Tester; the test frequency was 1.2 kHz.

## 3. Results and discussion

### 3.1. Particles' characterization

In model experiments it was found that polymeric latex particles stabilized by ionic surfactants or charged polymers are not suitable for deposition of conducting polymers. These tests resulted in the formation of "patchy" morphologies; no homogeneous shell formation was detected. Additionally, after deposition, polypyrrole dispersions became unstable and coagulation was observed even during pyrrole polymerization. This coagulation was caused mostly by enhanced sensitivity of ionic stabilizers to high ionic strength of reaction medium and partly due to the formation of secondary polypyrrole particles in solution. To avoid the above-mentioned problems, specially designed sterically stabilized polystyrene particles with a grafted poly(ethylene glycol) methacrylate (PEGMA) brush-like layer have been used as templates for polypyrrole deposition. Fig. 1a demonstrates that the hydrodynamic radius of PS–PEGMA particles can be effectively varied by fleet-ratio ($W_p/W_m$), the macroscopic weight ratio of polymeric stabilizer PEGMA ($W_p$) to styrene monomer ST ($W_m$).

Fig. 1a indicates that by addition of more PEGMA larger particle surface can be stabilized. This results in a decrease in the particle

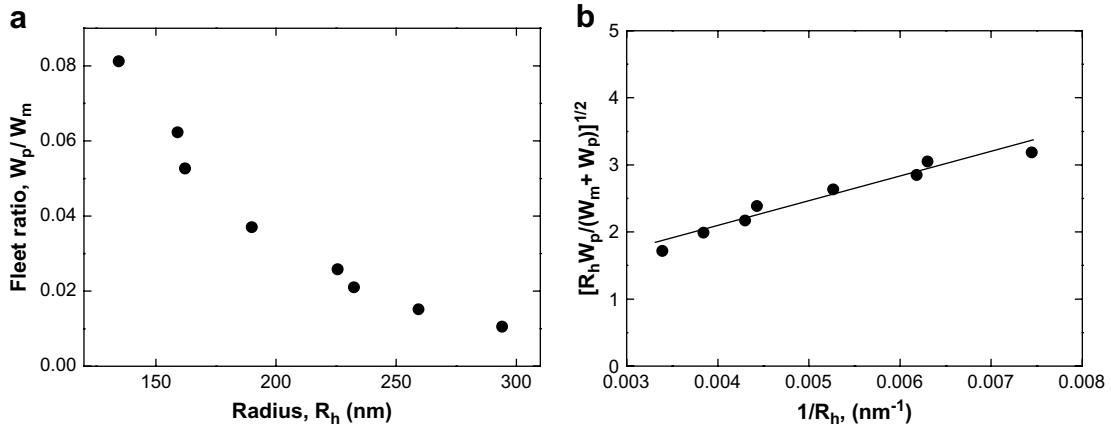


**Fig. 1.** (a) Fleet-ratio ($W_p/W_m$) dependence on the hydrodynamic radius ($R_h$) of PS–PEGMA particles. (b) Plot of $[RW_p/(W_m/W_p)]^{1/2}$ vs. ($1/R_h$) based on Eq. (1).

size. Recently Wu's group reported a structural model for surfactant/monomer microemulsion [29] and surfactant-free macromonomer/monomer emulsion [30,31] systems, which presented a quantitative relationship between the particle size and the fleet-ratio. This model suggests that for a given type of stabilizer and monomer, the surface area ($s$) occupied by each stabilizer molecule is the fundamental parameter for the control of the particle size. The relationship between the stabilizer/monomer fleet-ratio ($W_p/W_m$) and surface area ($s$) can be expressed by the following equation:

$$\left\{\frac{R_h W_p}{W_m + W_p}\right\}^{1/2} = \left[s\frac{N_A\rho}{3M_p}\right]^{-1/2}\left(1 - \frac{b}{2R_h}\right) \quad (1)$$

where $R_h$ is the hydrodynamic radius of the particles, $N_A$ is the Avogadro constant, $\rho$ is the average density of the microspheres, $M_p$ is the molar mass of the stabilizer and $b$ is the thickness of the stabilizer shell layer. From Eq. (1) follows that for constant $s$ the term $[R_hW_p/(W_m + W_p)]^{1/2}$ is also a constant for $b \ll 2R_h$. Applying Eq. (1) to our system we can conclude from Fig. 1b that the surface area occupied by PEGMA molecule on the particle surface is not constant. An increase in $[RW_p/(W_m + W_p)]^{1/2}$ when the PS–PEGMA particle size becomes smaller indicates that $s$ should decrease; this suggests that PEGMA molecules are more densely packed on the particle surface. This can result in an increase in the surface layer thickness $b$. From these considerations it can be concluded that the size of PS–PEGMA particles can be varied by changing the stabilizer/monomer fleet-ratio ($W_p/W_m$) and that the thickness of PEGMA-rich shell increases gradually when $R_h$ decreases. Based on these considerations samples prepared at different PEGMA contents were used for the deposition of PPy by the oxidative polymerization process.

Table 1 summarizes the ingredient amounts used for the preparation of composite particles as well as the final PPy loading in core–shell particles. Various experiments presented in Table 1 were performed to investigate the influence of the deposited polypyrrole amount, total surface area of PS–PEGMA particles and the thickness of PEGMA layer on the properties of final composites. Additional interesting parameter is the oxidant type, which determines the kinetics of the pyrrole polymerization, influences the morphology of PPy shell and controls the nature of dopant anion.

In the first set of samples (1–7) different polypyrrole amounts were deposited onto PS–PEGMA particles containing 2.5% PEGMA (particle diameter $R_h = 225$ nm). In the second set (samples 8–11) the loaded pyrrole amount was constant but particles with different PEGMA contents (1.5–12.5%) and different dimensions were applied as the core material. Finally, a few reactions were performed with similar core particles but different oxidation agents (samples 12 and 13 can be directly compared with sample 9).

**Table 1**
Preparation of composite particles

| No. | $R_h$ [nm] | PEGMA [wt%] | Latex [g] | Pyrrole [g] | Oxidant [g] | Water [g] | Loading $PPy^T$ [%] | Loading $PPy^P$ [%] | $SO_4^{2-}$ [%] |
|---|---|---|---|---|---|---|---|---|---|
| 1 | 225 | 2.5 | 40 | 0.1 | 0.5[a] | 160 | 2.5 | 2.28 | 0.05 |
| 2 | 225 | 2.5 | 40 | 0.2 | 1[a] | 160 | 5 | 4.5 | 0.13 |
| 3 | 225 | 2.5 | 40 | 0.3 | 1.5[a] | 160 | 7.5 | 6.41 | 0.29 |
| 4 | 225 | 2.5 | 40 | 0.4 | 2[a] | 160 | 10 | 9.38 | 0.56 |
| 5 | 225 | 2.5 | 40 | 0.5 | 2.5[a] | 160 | 12.5 | 11.06 | 0.78 |
| 6 | 225 | 2.5 | 40 | 0.6 | 3[a] | 160 | 15 | 13.4 | 0.74 |
| 7 | 225 | 2.5 | 40 | 1 | 5[a] | 160 | 25 | 19.29 | 1.27 |
| 8 | 229.5 | 1.5 | 40 | 0.2 | 1[a] | 160 | 5 | 4.86 | – |
| 9 | 162 | 5 | 40 | 0.2 | 1[a] | 160 | 5 | 4.69 | – |
| 10 | 134.4 | 7.5 | 40 | 0.2 | 1[a] | 160 | 5 | 4.93 | – |
| 11 | 152.3 | 12.5 | 40 | 0.2 | 1[a] | 160 | 5 | 4.9 | – |
| 12[d] | 162 | 5 | 40 | 0.2 | 1[b] | 160 | 5 | 3.5 | – |
| 13[d] | 162 | 5 | 40 | 0.2 | 1[c] | 160 | 5 | 1.2 | – |
| 14[d] | 162 | 5 | 20 | 0.3 | 1.5[a] | 20 | 15 | 12.83 | – |
| 15[d] | 162 | 5 | 20 | 0.3 | 1.5[b] | 20 | 15 | 8.83 | – |
| 16[d] | 162 | 5 | 20 | 0.3 | 1.5[c] | 20 | 15 | 2.10 | – |

[a] $Na_2S_2O_8$.
[b] $FeCl_3$.
[c] $H_3PMo_{12}O_{40}\cdot 29H_2O$.
[d] Runs 12–16 were terminated after 40 min (other runs, 1–11, were terminated after 6 h).

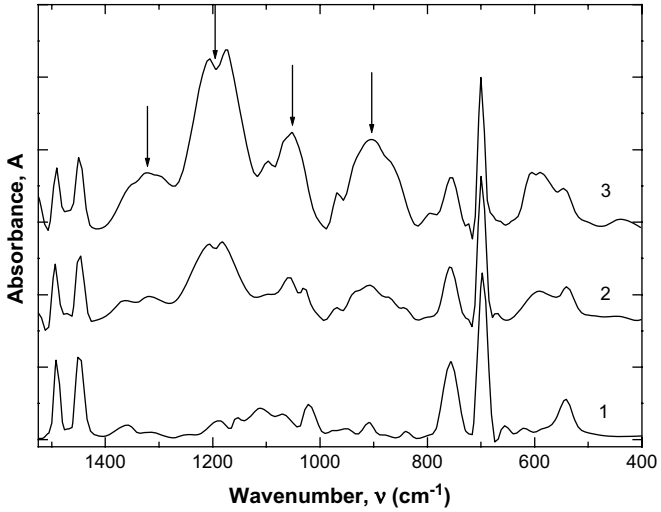


**Fig. 2.** FTIR spectra of PS–PEGMA core (1) and composite particles with loaded 4.5% (2) and 6.41% (3) polypyrrole.

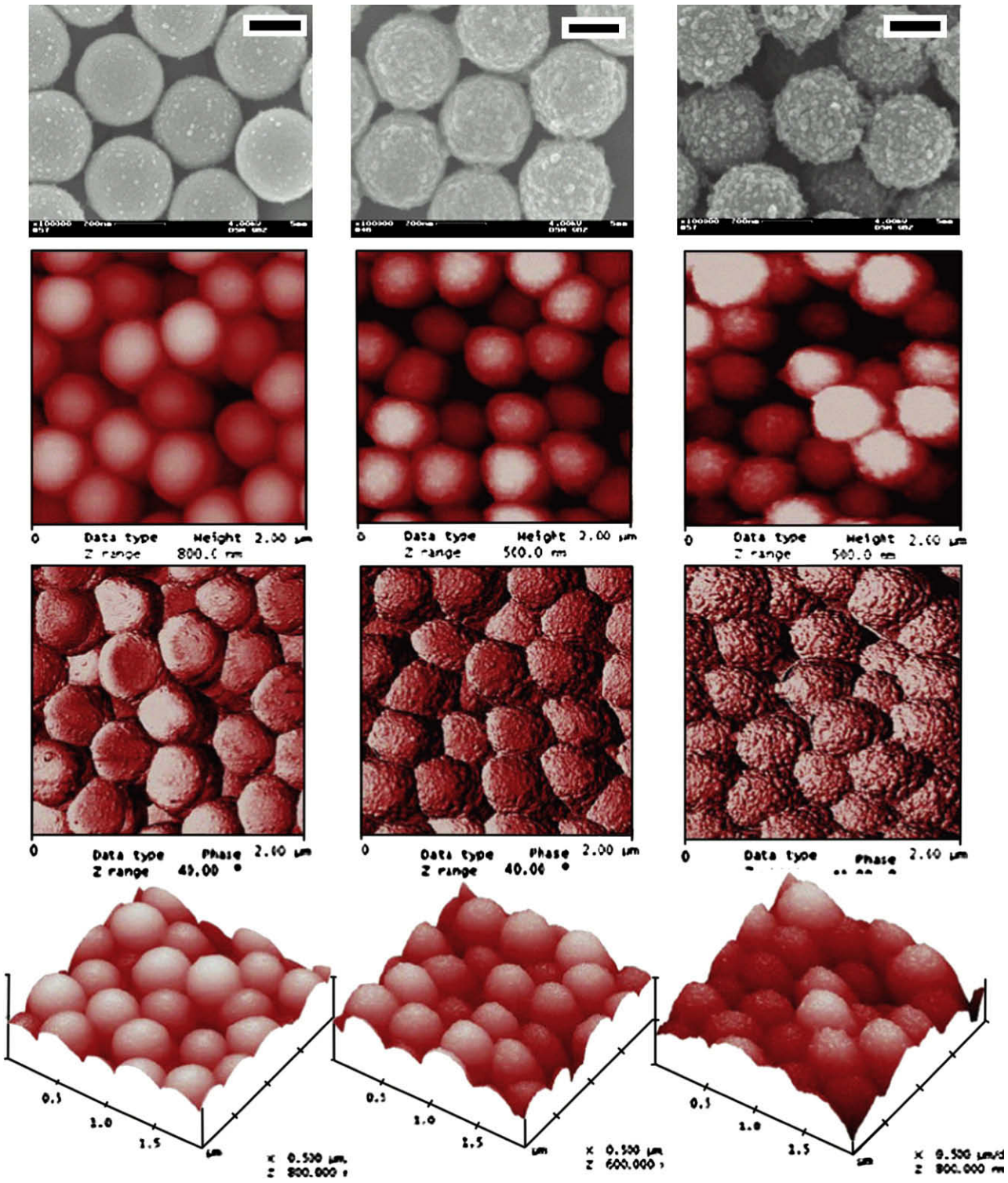


**Fig. 3.** SEM and AFM images of PS–PEGMA particles coated with PPy amounts 2.5, 5 and 7.5%. SEM micrographs (1st row); AFM images made in the tapping mode (height images – 2nd row; phase images – 3rd row; and 3D height images – 4th row) (from left to right the PPy amount increases). The height, phase, and 3D height scales are 0–500 nm, 0–40°, and 0–800 nm, respectively. The lateral dimensions of AFM scans were $2 \times 2$ µm, the scale of SEM is given by black bar, which represents 200 nm.

Samples 14–16 were prepared in order to study the polymerization kinetics.

The amount of polypyrrole (PPy) in composite particles presented in Table 1 was determined by elemental analysis. Comparison of the theoretically expected values ($PPy^T$) with the experimental data ($PPy^P$) indicated that in all cases the pyrrole polymerization was very effective. The samples prepared with $FeCl_3$ and $H_3PMo_{12}O_{40} \cdot 29H_2O$ showed lower PPy loadings because the reactions were terminated before all pyrrole was consumed. The loaded PPy amount could be increased by reducing the amount of core particles in the system and keeping the initial pyrrole concentration constant (see samples 14–16).

The deposition of polypyrrole on the PS–PEGMA particle surface was detected by FTIR spectroscopy. Fig. 2 shows a part of FTIR

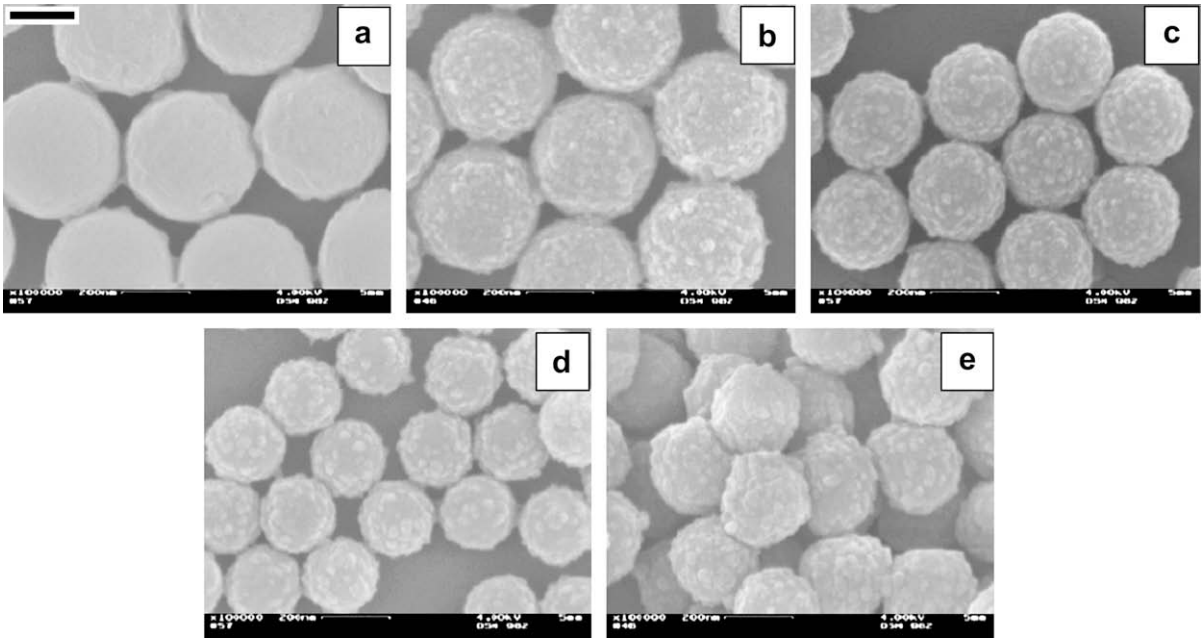


**Fig. 4.** SEM images of samples 8 (a), 2 (b), 9 (c), 10 (d), and 11 (e) (cf. Table 1). The scale of all photographs is given by black bar in (a), which represents 200 nm.

spectra (1500–400 $cm^{-1}$) of samples prepared using $Na_2S_2O_8$ as oxidant with PPy loadings 4.5% and 6.41%.

The presence of PPy in composites is documented by characteristic peaks marked by arrows. The band of the C–N stretching vibration in the ring should appear at 1459 $cm^{-1}$, but it is overlapped by the doublet of the C–H bending vibration of polystyrene. The broad band 1400–1275 $cm^{-1}$ is attributed to the C–H or C–N in-plane deformation modes (maximum located at 1322 $cm^{-1}$). The broad signal 1250–1140 $cm^{-1}$ corresponds to breathing vibration of the pyrrole ring (maximum at 1200 $cm^{-1}$). In-plane deformation vibration of $NH_2^+$ which is formed due to protonation of PPy chains shows a peak at 1100 $cm^{-1}$ [32]. Peaks at 1037 and 910 $cm^{-1}$ correspond to N–H in-plane and C–C out-of-plane ring deformation vibration, respectively. It can be also observed that typical polystyrene doublet signals at 1495–1453 $cm^{-1}$ (C–H bending vibration) and 754–699 $cm^{-1}$ (C–H out-of-plane bending) are smaller if PPy loading increases.

SEM images of samples prepared at different PPy loadings are presented in Fig. 3. These microscopy images clearly demonstrate that more and more PPy inclusions appear on the particle surface as PPy load increases. It is also clear that the surface roughness of the composite particles increases. PPy is deposited in the form of very small "islands" which are located at a certain distance from each other if the PPy loading is low (see the sample with lowest PPy content) and then become more tightly packed at high PPy loadings. Actually, this polypyrrole shell possesses a complex structure of self-assembled PPy nanoparticles. It can also be observed that at higher PPy loadings the size of PPy domains increases. This effect can be related to the direction of shell growth: at low PPy loadings its inclusions spread on the PS–PEGMA particle surface; and a further increase of the size of PPy domains induces more and more compact packing of PPy inclusions. When the particle surface

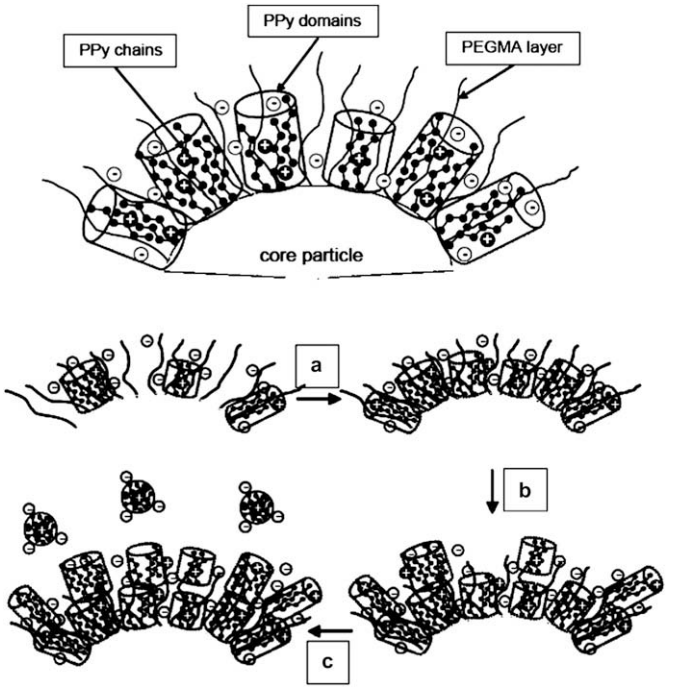


**Fig. 5.** Schematic representation of surface layer formed on particle surface (top) and morphology evolution with increasing PPy loading (bottom).

**Table 2**
Hydrodynamic radii of core $R_h^c$ and core–shell $R_h^{c-s}$ particles, thicknesses of shell layers $H$ and PPy loadings for various samples

| No. | PEGMA [wt%] | $R_h^c$ [nm] | $R_h^{c-s}$ [nm] | $H$ [nm] | Loading $PPy^P$ [%] |
|---|---|---|---|---|---|
| 1 | 2.5 | 193 | 193 | 0 | 2.28 |
| 2 | 2.5 | 193 | 194.3 | 1.3 | 4.5 |
| 3 | 2.5 | 193 | 195.3 | 2.3 | 6.41 |
| 4 | 2.5 | 193 | 195.6 | 2.6 | 9.38 |
| 5 | 2.5 | 193 | 197.6 | 4.6 | 11.06 |
| 6 | 2.5 | 193 | 202 | 9 | 13.4 |
| 7 | 2.5 | 193 | 202.1 | 9.1 | 19.29 |
| 8 | 1.5 | 211 | 211 | – | 4.86 |
| 9 | 5.0 | 153 | 154.4 | 1.4 | 4.69 |
| 10 | 7.5 | 118 | 121.2 | 3.2 | 4.93 |
| 11 | 12.5 | 130 | 133.9 | 3.9 | 4.9 |
| 14 | 5.0 | 153 | 156.7 | 3.7 | 12.83 |
| 15 | 5.0 | 153 | 156 | 3 | 8.83 |
| 16 | 5.0 | 153 | 153 | – | 2.10 |

The sample numbering follows the numbering used in Table 1.

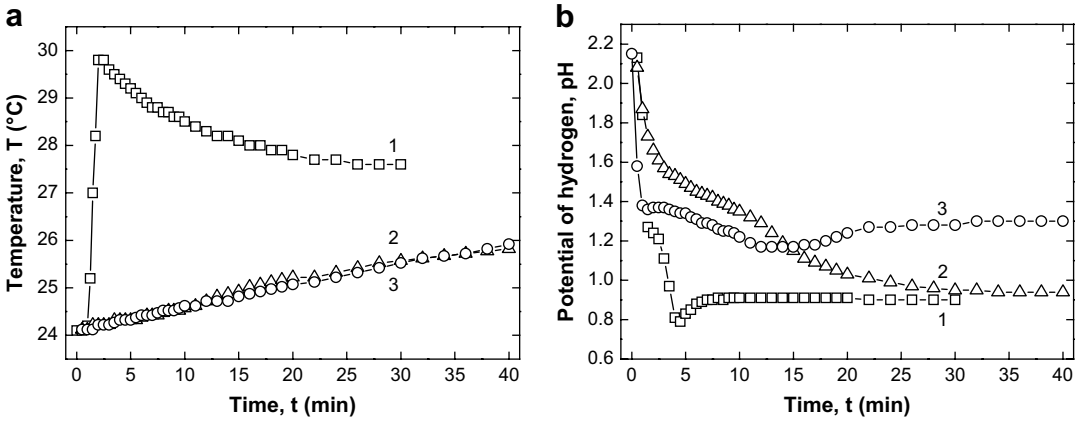


**Fig. 6.** Temperature profile of the exothermic oxidation of pyrrole in the presence of PS–PEGMA particles (a); and pH change during the formation of composite particles (b) in the presence of different oxidants (1 – $Na_2S_2O_8$ (sample 14); 2 – $FeCl_3$ (sample 15); 3 – $H_3PMo_{12}O_{40}\cdot 29H_2O$ (sample 16)).

has been completely covered with the first layer of PPy domains, the shell starts to grow in the direction perpendicular to particle surface. Under these conditions polypyrrole particles can form larger aggregates, which are clearly visible on microscopy images (see Fig. 3, sample with 7.5% PPy), inducing an increase in the surface roughness of composite particles. Additionally, at higher PPy loadings (starting from 12.5%) the formation of secondary polypyrrole particles was detected (data not shown). These secondary particles are not attached to the PS–PEGMA core surface and cause partial destabilization of the colloidal system by formation of flocks in water solution.

Fig. 4 presents SEM images of the samples prepared with similar PPy loadings, but PS–PEGMA particles of different size have been used as a template.

The microphotographs indicate that the particle morphology can be influenced by the particle size and by the total particle surface area in the system. Smaller PS–PEGMA particles possess a much larger surface area in a certain volume of the dispersion, compared with larger microspheres. It follows from the images presented in Fig. 4: if we increase the total particle surface area in the system and load the same PPy amount, the morphology of the PPy layer changes from more or less compact to "patchy". It was also mentioned above that the thickness of the PEGMA layer on the particle surface should increase for smaller PS–PEGMA particles. The increased graft density of the PEGMA chains on the polystyrene particle surface probably inhibits the growth of PPy domains within this hydrophilic layer [33,34].

Based on the experimental results mentioned above, the process of PPy deposition on the core particles can be presented as schematically shown in Fig. 5. Considering the morphology of the surface layer of PS–PEGMA particles, it can be assumed that deposition of PPy chains into defined domains of grafted PEGMA-brush layer of the polymeric template leads to strongly directed layer growth.

The PPy macromolecules possess a positive charge in the oxidized state, which is counterbalanced by anions from the oxidizing agent, and can form small nanodomains visible in SEM due to the partial phase separation on the latex particle surface after water removal. Based on microscopy investigations presented in Fig. 3, it can be suggested that the increase in PPy loading induces the shell growth in lateral direction (Fig. 5a), which results in the step-wise coverage of the latex particle surface. During this step the shell thickness does not increase considerably. After the saturation point has been reached, PPy shell starts to grow in perpendicular direction (Fig. 5b) and the surface roughness and shell thickness are rising. Finally, if the stabilizing capacity of PEGMA layer is reached at high PPy loadings, secondary particles appear in the system (Fig. 5c). A special feature of the obtained composite particles is that organized spherical PPy domains on the PS–PEGMA particle surface cannot be removed by washing or water evaporation, since PEGMA chains are covalently bound to the PS-core surface and no desorption processes take place as in the case of water-soluble polymer stabilizers. Moreover, the PPy is high surface energy material and its domains hold together due to strong PPy–PPy interactions [35].

Table 2 shows some representative particle radii of PS–PEGMA and corresponding composite particles as analyzed from SEM pictures. The increase in PPy loading (samples 1–7) leads to the formation of thicker shells. The shell thickness in the case of samples prepared with similar PPy loadings, but using the core of a different size (samples 8, 9, 10, and 11), increases gradually if the particle size decreases. This result also correlates with the

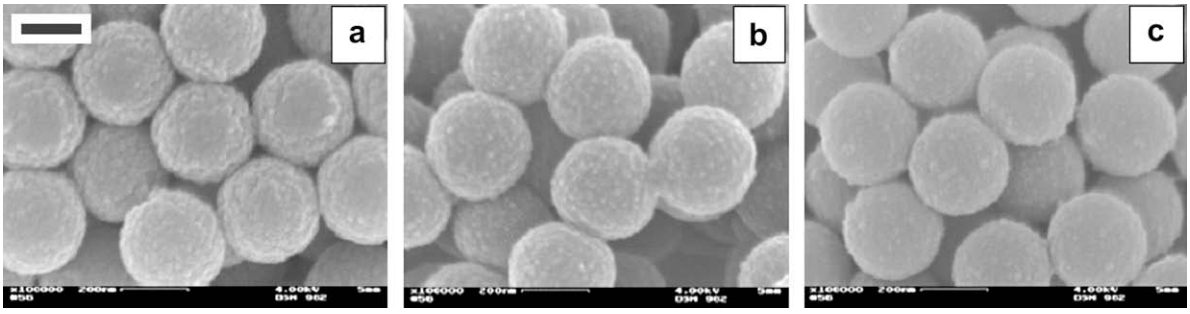


**Fig. 7.** SEM images of composite particles prepared with different oxidants ((a) – $Na_2S_2O_8$ (sample 14); (b) – $FeCl_3$ (sample 15); (c) – $H_3PMo_{12}O_{40}\cdot 29H_2O$ (sample 16)). The scale of all photographs is given by black bar in (a), which represents 200 nm.

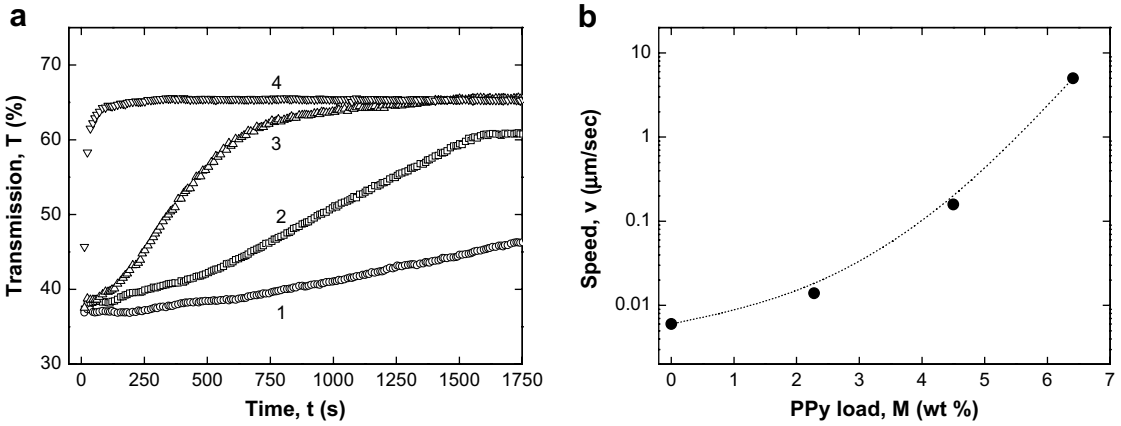


**Fig. 8.** Sedimentation curves for samples with different PPy loadings (1 – no PPy, 2 – 2.28%, 3 – 4.5% and 4 – 6.41%) at 2000 rpm (a); and calculated sedimentation velocity $v$ as a function of PPy loading (b).

microscopy investigations presented; the increase in surface roughness in the case of smaller particles leads to a somewhat larger shell thickness *H*. Additionally, at higher PPy loads (starting from 11.06%) formation of secondary polypyrrole particles was detected. These secondary particles are not attached to the PS–PEGMA core surface and cause partial destabilization of colloidal system by formation of flocks in water solution.

To demonstrate an alternative way of controlling the thickness of polypyrrole shell on the PS–PEGMA particle surface, various oxidants were selected; they can influence the polymerization rate of pyrrole. We selected $FeCl_3$ [16,36–38] and $H_3PMo_{12}O_{40}\cdot 29H_2O$ [39] as common oxidants for pyrrole. Fig. 6a shows the exothermic profiles of the pyrrole oxidation process. It is interesting to note that in the pyrrole polymerization in the presence of $Na_2S_2O_8$ temperature increases very rapidly and after PPy has been produced, the reaction mixture slowly cools. Similar temperature profiles were reported by Stejskal et al. [40,41] for aniline polymerization. In these studies polymerizations were also completed during 5–7 min. In contrast, the reactions performed with $FeCl_3$ and $H_3PMo_{12}O_{40}\cdot 29H_2O$ exhibit totally different temperature profiles. In these cases temperature increases monotonically as the polymerizations proceed and polymerization rates seem to be much lower than in the case of $Na_2S_2O_8$-initiated reaction. The progress of polymerization can also be monitored by pH measurements [42,43] (see Fig. 6b). The locally increased concentration of protons at the electrode surface is responsible for the overshooting to low pH values and for observation of the minimum. When polymerization is complete, the concentration of protons equilibrates and pH slightly increases; then it remains constant. It was observed that the minimum pH correlates with maximum temperature in the $Na_2S_2O_8$-initiated polymerization. In the reactions performed with $FeCl_3$ and molybdate, these minima are not clearly pronounced, probably due to a slower oxidation process.

Different kinetics of the pyrrole polymerization with different oxidants, demonstrated in Fig. 6, can be used for the control of polypyrrole shell thickness on the PS–PEGMA surface. For example, reaction processes shown in Fig. 6 were terminated after 40 min and composite particles with different PPy loadings could be obtained (see Table 1; samples 9, 12, and 13 possess PPy load 4.69, 3.5, and 1.2%, respectively, and samples 14–16 exhibit PPy loadings 12.83, 8.83, and 2.10%, respectively). Additionally, polypyrrole chains in every case are doped with different anions without any great changes in particle morphology.

The SEM images presented in Fig. 7 indicate that PS–PEGMA cores are homogeneously coated with polypyrrole, independently of the oxidation agent. The thickness of the polypyrrole layer deposited on the PS core increases gradually with PPy loading (see samples 14–16 in Table 2). The shell thicknesses of samples 12, 13 and 16 could not be determined due to very low PPy loading.

For the fabrication of thin films by the controlled particle deposition the colloidal stability is of great importance. The particle behaviour in the continuous phase (such as aggregate formation, sedimentation) determines to some extent the film quality. For that reason the sedimentation of PS–PEGMA particles with deposited PPy shells was investigated by analytical centrifugation [44]. In this device an integrated optoelectronic sensor system allowed to detect spatial and temporal changes of light transmission during rotation. Throughout the measurement, transmission profiles were recorded and sedimentation processes could be depicted as a time course of the relative position of the boundary between supernatant and sediment (resolution better than 100 μm). The transmission–time curves for particles bearing different polypyrrole amounts (samples 1–3) are presented in Fig. 8a. The transmission increases with the centrifugation time since particles move to the bottom of the cell. The slope of the transmission–time curves was used to calculate the sedimentation velocity (Fig. 8b).

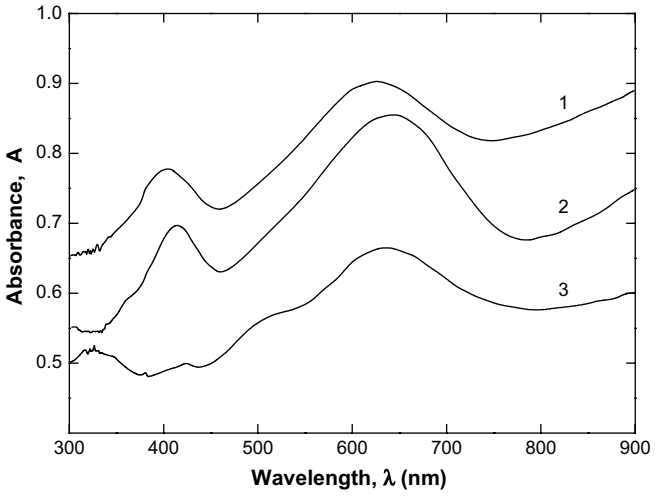


**Fig. 9.** Absorption spectra of thin films prepared from PEGMA (core)–PPy (shell prepared with different oxidants): (1) $Na_2S_2O_8$ (sample 14, viz. Table 1), (2) $FeCl_3$ (sample 15), (3) $H_3PMo_{12}O_{40}\cdot 29H_2O$ (sample 16). Spectra are not corrected for the PPy shell thicknesses.

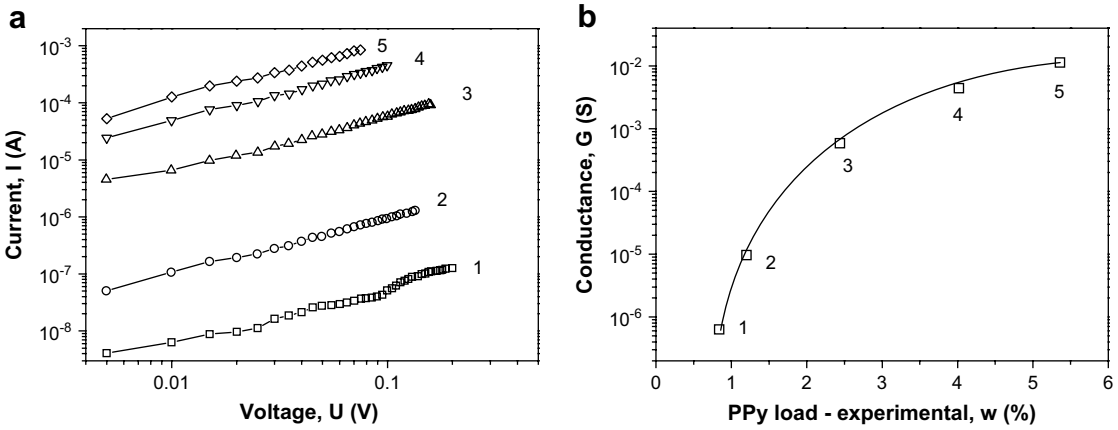


**Fig. 10.** Current–voltage characteristics (a) and the dependence of film conductance (b) on the level of PPy loading (oxidant $H_3PMo_{12}O_{40}\cdot 29H_2O$). Dependence (1) – loading level of PPy 0.8 wt%, (2) – 1.2 wt%, (3) – 2.4 wt%, (4) – 4.1 wt%, (5) – 5.4 wt%.

When larger PPy amount is deposited on PS–PEGMA particle surface the sedimentation velocity increases.

The incorporation of polypyrrole into PEGMA-rich shell leads initially to partial "immobilization" of PEGMA chains by formation of hydrogen bonds. Later on, when the shell layer is saturated and PPy amount is still increasing, PEGMA chains are totally blocked by polypyrrole. Since PS–PEGMA particles' colloids are stabilized mostly by the steric mechanism mentioned above, PPy inclusions considerably reduce the colloidal stability of the composites.

### 3.2. Electrical properties

The absorption spectra of deposited films are shown in Fig. 9. Character of the spectra is independent of the type of oxidant. The spectra consist of two bands with the maxima located at about 400 and 640 nm. These peaks are characteristic for PPy absorption. Note that absorbance increases with the PPy content. Usually, the long wavelength part of the spectrum is used for the determination of the energy gap of the material. However, in our cases the scattering processes are quite strong and we are not able to determine the right cross-over point with $x$-axis. Direct measurement of the temperature dependence of the current gives the activation energy about $E_a = 0.17$ eV (oxidant $FeCl_3$, gap electrode configuration). It suggests quite high doping level.

The value of resistivity obtained for films of different thicknesses was found to be $34 \pm 2\ \Omega$m (oxidant $FeCl_3$, PPy loading 9%) as obtained by four-point-probe technique. The current and therefore layer conductivity depended on the PPy loading level $w$, as follows from Fig. 10, especially for low $w$.

For higher loading levels ($w > 4\%$) a tendency to saturation was observed. Note that for loading levels lower than 1% the film conductivity was quite low and PPy shells discontinuous. It this case a pre-contact potential barrier and/or barriers among core–shell particles were observed, especially when the measurements were performed in air (see Fig. 11). The current limitation in the voltage region 1–3 V, which suggests the presence of the barrier, is evident. At higher temperatures the barrier effect was more pronounced. In vacuum the barrier effect was weaker, but still the shape of the current–voltage characteristic suggested the presence of the barrier (exponential dependence of the current on voltage).

Curve 2 in Fig. 11 can be analyzed as follows.

The "quasi" ohmic character of the current with a weak slope increase at low voltages is followed by the $j \sim U^3$ dependence for voltages higher than 4 V (sample thickness was 190 nm). It suggests charge injection from ITO electrode [45]. The low-voltage part of the characteristic is typical of a contact-limited current, where the potential barrier at the contact strongly limits the electric current. Among the core–shell particles charge carrier traps of structural origin can be assumed. Thus, the trapping processes related to the charge crossing the barrier must be taken into account. Therefore, the model of contact-limited currents with charge carrier trapping in the barrier seems to be suitable for the explanation of the shape of the low-voltage $I \sim U$ dependence (note the loading PPy level was quite low).

The thermionic emission equation is given by equation [43]:

$$j \approx A_0 \exp\left(-\frac{E_0}{kT}\right) \exp\left\{-\left[-e\int_0^{x_m} F(x)\mathrm{d}x - \frac{e^2}{16\pi\varepsilon_0\varepsilon x_m}\right] \Big/ kT\right\} \qquad (2)$$

with the second exponential term denoting the probability of a carrier to overcome the potential barrier formed by the superposition of the image Coulombic, space charge and external potentials in the sample. Here, $j$ is the current density, $E_0$ is the surface energy of the carrier, $F(x)$ is the electric field at distance $x$ from the contact, $A_0$ is the constant, $k$ is the Boltzmann constant, $T$ is the absolute temperature, $e$ is the unit charge, $x_m$ is the position of barrier maximum at the applied voltage and $\varepsilon\varepsilon_0$ is the electric permittivity.

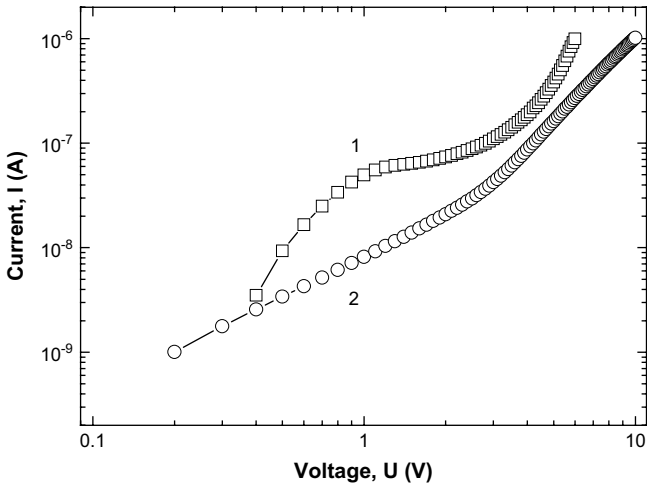


**Fig. 11.** Current–voltage characteristics of ITO/core–shell layer/Al sample in air (curve 1, squares) and in vacuum (curve 2, open circles). Oxidant: $H_3PMo_{12}O_{40}\cdot 29H_2O$ (see sample 13 in Table 1).

The condition of electric neutrality causes the system to be divided into two regions, with $x_m$ as the boundary at which the electric field $F(x_m) = 0$ and the potential between the electrodes has its maximum $\phi_m$. When the voltage applied to the electrodes increases, $x_m$ moves towards the injecting electrode and $\phi_m$ decreases [46,47]. As the voltage increases further, the barrier height can no longer be lowered by the removal of opposite charge from the injecting electrode and the barrier lowering takes place by the interaction of the image force with the applied field (Schottky effect, [48]). The current becomes contact- or emission-limited (ELC) rather than bulk limited. However, due to a large number of traps present in the insulator, the space charge still exists; its influence on the ELC $j$–$U$ characteristic was considered by Frank and Simmons [46]. They also assumed that traps modify, depending on the electric field, the ratio of free and trapped charge densities. For a carrier to reach the potential maximum without being trapped by charge traps, it must have a diffusion length $l_d$ greater than the distance $x_m$, to the potential maximum. If $l_d \ll x_m$, the current is reduced and its field dependence is influenced by a field shortening the distance $x_m$.

However, only a fraction of injected carriers (holes in our case) will reach the maximum of the barrier due to trapping in the region $0 < x < x_m$, where in the distance $x = 0$ an injection electrode is located. Since the probability $P$ of a carrier for not being trapped is [49]

$$P = \exp(-x_m/l_d) \tag{3}$$

it follows for the current from Eqs. (2) and (3)

$$j \approx j_0 \exp\left\{ -\left[ -e\int_0^{x_m} F(x)\mathrm{d}x - \frac{e^2}{16\pi\varepsilon_0\varepsilon x_m}\right] \Big/ kT - \frac{x_m}{l_d}\right\} \tag{4}$$

If space-charge effects are negligible,

$$F(x_m) = \frac{e}{16\pi\varepsilon\varepsilon_0 x_m^2} \tag{5}$$

$$x_m \approx \left(\frac{ed}{16\pi\varepsilon\varepsilon_0 U}\right)^{1/2} \tag{6}$$

coincide with the position of the Schottky barrier [50] simplifying Eq. (4) to the form [49]

$$j \approx j_0 \exp\left\{ \left[\frac{eUx_m}{d} + \frac{e^2}{16\pi\varepsilon\varepsilon_0 x_m}\right] \Big/ kT - \frac{x_m}{l_d}\right\} \tag{7}$$

Here $j_0$ is the constant, $U$ is the applied voltage and $d$ is the sample thickness.

The basic relations for charge carrier transport are:

$$l_d = (D\tau)^{1/2} \tag{8}$$

$$D = \mu kT/e \tag{9}$$

$$\tau = (N_t v_{th}\vartheta)^{-1} \tag{10}$$

where $D$ is the diffusion coefficient, $\tau$ is the lifetime of free charge carriers, $\mu$ is the charge mobility, $N_t$ is the trap concentration, $v_{th}$ stands for the thermal velocity of the carriers and $\vartheta$ for the cross-section of the carrier trapping.

By introducing Eqs. (8)–(10) into Eq. (7) we can get

$$j \approx j_0 \exp\left(aU^{1/2} - bU^{-1/2}\right) \tag{11}$$

where

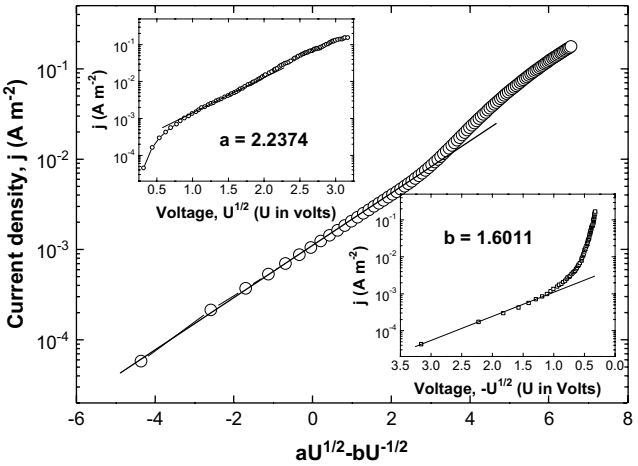


**Fig. 12.** $I \sim U$ characteristics of ITO/core–shell layer/Al sandwich sample in vacuum. Oxidant: $H_3PMo_{12}O_{40}\cdot 29H_2O$.

$$a = \frac{e}{kT}\left(\frac{e}{4\pi\varepsilon\varepsilon_0 d}\right)^{1/2} \tag{12}$$

and

$$b = e\left(\frac{dN_t v_{th}\vartheta}{16\pi\varepsilon\varepsilon_0\mu kT}\right)^{1/2} \tag{13}$$

According to Eq. (11) the current is driven by two processes: the lowering of the Schottky barrier at higher voltages which is proportional to $U^{1/2}$ (thus $j \sim \exp(aU^{1/2})$, see Fig. 12, top inset) and the trap control of the number of carriers arriving at the barrier with sufficient energy to cross it (for low voltages $j \sim \exp(-bU^{-1/2})$; Fig. 12, bottom inset). The plot ln $j$ vs. $(aU^{1/2} - bU^{-1/2})$ is also given in Fig. 12. The experimental characteristic gives a good agreement with the proposed model. For high voltages we assume that the traps are filled, the barrier is low, the current strongly increases and transition into the space-charge-limited (SCL) injection is observed. Here, the current–voltage characteristic is of the type $j \sim U^n$, $n \geq 2$ [45].

The PPy load concentration mentioned above influences the thickness of the shell cover. The dependence is nearly linear with the slope 0.5 (shell thickness vs. PPy percentage load). Note that the value of the conductivity depends on the type of oxidant. The resistivity of films prepared using $Na_2S_2O_8$ oxidant was three times higher

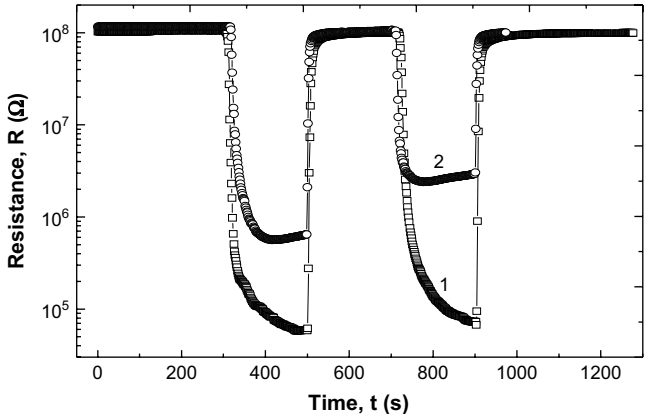


**Fig. 13.** Change in the impedance of films prepared with $H_3PMo_{12}O_{40}\cdot 29H_2O$ oxidant (curve 1) and with $FeCl_3$ oxidant (curve 2) during the change of relative humidity from 50 to 96%.

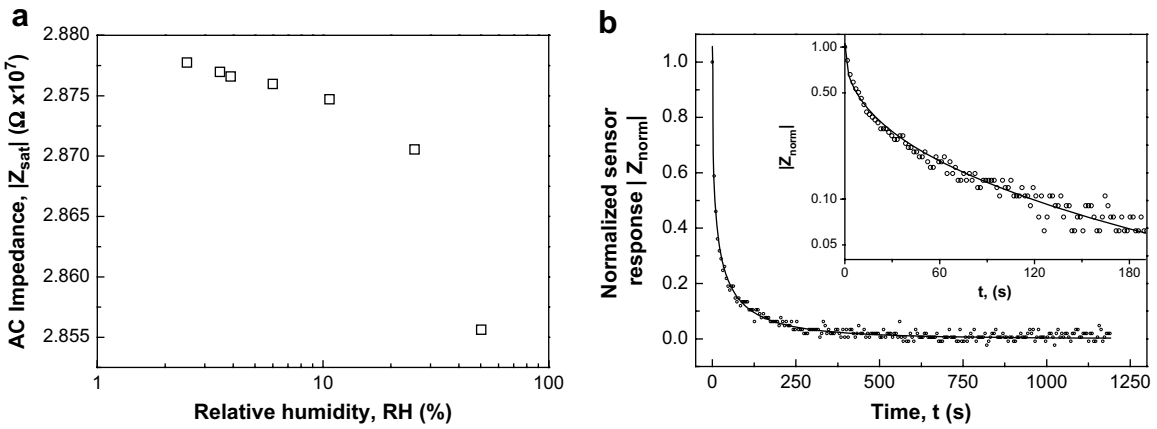


**Fig. 14.** (a) Sensitivity of the humidity sensor based on film of core–shell particles prepared with $H_3PMo_{12}O_{40}\cdot 29H_2O$ oxidant. (b) Analysis of sensor response kinetic (normalized impedance $|Z_{norm}|$) towards abrupt relative humidity change from 2.3 to 10.7% (at time $t = 0$). The early part of the kinetic in semilogarithmic scale is shown in the inset. The solid line represents the best fit of stretched exponential function to the experimental data.

(cf. resistivity of layers prepared using $FeCl_3$ oxidant which was $34 \pm 2\ \Omega$m at the same loading level). The lowest resistivity was found for films prepared using $H_3PMo_{12}O_{40}\cdot 29H_2O$ oxidant; here the value was nearly one order of magnitude lower than that obtained for films prepared using $FeCl_3$ oxidant at the same loading level.

The conductivity of the particles under study prepared with $H_3PMo_{12}O_{40}\cdot 29H_2O$ oxidant was, in contrast to those prepared with $FeCl_3$ oxidant, very stable to humidity. The changes of the resistance for relative humidity changes from 50 to 96% (fast change during ca. 2 s realized by switching between semi-dry and wet flowing nitrogen) are given in Fig. 13. The resistance change was more than three orders of magnitude (thickness of the film was ca. 200 nm); for thinner layers even greater changes were detected. The sensitivity to humidity can be ascribed to the dissociation process of PPy and anion, which influences ionic conductivity of the system. Therefore, it can be concluded that the obtained core–shell particles are suitable for the fabrication of humidity sensors.

The humidity sensing properties of the prototype sensor based on the film consisting of core–shell particles prepared with $H_3PMo_{12}O_{40}\cdot 29H_2O$ oxidant are shown in Fig. 14. The dependence of sensor impedance $|Z_{sat}|$ saturated at relative humidity levels ranging from 2.3 to 50% in Fig. 14a reveals two regions of the sensor function. For RH lower than 50% we obtained nearly linear response with rather small magnitude of impedance change. When RH is increasing above this level, the impedance begins to decrease faster. Finally, when changing RH from 80 to 96% the impedance decreases by about three orders of magnitude ($|Z_{sat}|$ changes from 27 MΩ to 56 kΩ). Similar behaviour was observed by the other authors [51] for sensors based on PPy thin film.

One can compare this behaviour to that of ceramic humidity sensors. In ceramics, the humidity response is considered to occur in two stages [52]: at low relative humidity, adsorption and dissociation of water molecules take place, forming hydroxyl ions at the positively charged sites (at the oxidized polypyrrole chain, in our case). Further adsorption leads to the formation of hydroxonium, protonic transport to adjacent sites and an increase of conductivity (ionic). At high relative humidity (e.g., RH > 40%), the water vapour condenses in the capillary-like pores, forming liquid-like layer. A further rise in electrical conductivity occurs due to electrolytic conduction.

The intrinsic electronic conductivity in our material is low enough to allow us to observe contribution of $H^+$ and $H_3O^+$ ions' transport to the conduction, and porosity of the film allows for creation of condensed water channels; thus we incline to support the above-mentioned hypothesis.

The sensor signal evolution in time for abrupt RH change from 2.3 to 10.7% is shown in Fig. 14b. This is the representative example for the behaviour of the sensor in the region of RH below 50%. The saturated value of the impedance $|Z_{sat}|$ was subtracted from the experimental data. The resulting data, normalized to one (yielding $|Z_{norm}|$ quantity), can be modeled by stretched exponential function (solid line Fig. 14b):

$$|Z_{norm}(t)| = \frac{|Z(t)| - |Z_{sat}|}{|Z(t=0)|} = \exp\left\{-(t/\tau)^{\beta}\right\} \quad (14)$$

where $t$ is the time, $\tau$ is the time constant and $\beta$ is the parameter describing the deviation from the purely exponential decay; $0 < \beta < 1$. In our case $\beta = 0.42$. For the longer times (greater than 30 s) the behaviour can be approximated by single exponential decay function with characteristic time $\tau_0 = 90$ s. The $\tau_0$ values in this RH region vary from 80 to 150 s.

The use of the composite particles coated with PPy shell as building blocks for the preparation of gas-sensitive layers offers several advantages compared to the compact conducting polymer layers. Firstly, the sensing material (PPy) is distributed in the form of nanolayers and is easily accessible to analyte molecules due to the interparticle voids formed after the composite particles come into contact. Secondly, such layers offer an enormous surface area, which results in higher sensor sensitivity. Thirdly, the proposed technology is very flexible and allows introduction of other intrinsically conducting polymers such as polythiophenes or polyanilines and variation of their electrical properties by controlling the polymerization process in colloidal systems.

## 4. Conclusion

Monodisperse PS–PEGMA particles have been used as a template for deposition of polypyrrole (PPy). The obtained composite particles possess core–shell morphology where the shell is composed of small PPy nanodomains. It has been demonstrated that the PEGMA-rich shell layer on the template surface has enhanced the affinity to polypyrrole chains, providing an excellent possibility to control the morphology and thickness of the PPy shell. The shell thickness can be varied by changing PPy loading and by influencing the pyrrole polymerization kinetics in the presence of different oxidants. The last method provides also the incorporation of different anions into polypyrrole shell.

The type of anions influences the electrical conductivity of the particles, which among others, depends on the polypyrrole content

and morphology of films. The highest electrical conductivity was obtained for films prepared using $FeCl_3$ as oxidant. Current–voltage dependences of the films prepared from the core–shell particles with low PPy shell loading were characteristic of contact-limited currents. At higher voltages, a charge carrier injection was observed. The conductivity changes with humidity allowed us to use the material for the humidity detection.

## Acknowledgements

The authors are thankful to Mrs. E. Kern for SEM measurements and the Deutsche Forschungsgemeinschaft (DFG) for financial support of collaboration research project SFB 287 "Reactive Polymers". The financial support by grant No. KAN400720701 from Grant agency of the Academy of Sciences of the Czech Republic and by the Ministry of Education, Youth and Sports of the Czech Republic (COST grant No. 1041/2006-32) is also gratefully appreciated.

## References

[1] Cao Y, Andreatta A, Heeger AJ, Smith P. Polymer 1989;30:2305.
[2] Lacroix JC, Kanazawa K, Diaz AF. J Electrochem Soc 1989;136:1308.
[3] Bousalem S, Mangeney C, Chehimi MM, Basinska T, Miksa B, Slomkowski S. Colloid Polym Sci 2004;282:1301.
[4] Mangeney C, Bousalem S, Connan C, Vaulay M-J, Bernard S, Chehimi MM. Langmuir 2006;22:1301.
[5] DeArmitt C, Armes SP. Langmuir 1993;9:652.
[6] Luk SY, Lineton W, Keane M, DeArmitt C, Armes SP. J Chem Soc Faraday Trans 1995;91:905.
[7] Fujii S, Armes SP, Jeans R, Devonshire R, Warren S, McArthur SL, et al. Chem Mater 2006;18:2758.
[8] Cairns DB, Khan MA, Perruchot C, Riede A, Armes SP. Chem Mater 2003;15:233.
[9] Odegard R, Skotheim TA, Lee HS. J Electrochem Soc 1991;138:2930.
[10] Armes SP, Aldissi M. Polymer 1990;31:569.
[11] Beadle PM, Rowan L, Mykytiuk J, Billingham NC, Armes SP. Polymer 1993;34:1561.
[12] Beaan M, Armes SP. Colloid Polym Sci 1993;271:70.
[13] Digar ML, Bhattacharyya SN, Mandal BM. Polymer 1994;35:377.
[14] Mandal TK, Mandal BM. Polymer 1995;36:1911.
[15] Mandal TK, Mandal BM. J Polym Sci Part A Polym Chem 1999;37:3723.
[16] Simmons MR, Chaloner PA, Armes SP. Langmuir 1995;11:4222.
[17] Qi Z, Pickup PG. Chem Mater 1997;9:2934.
[18] Slimane AB, Chehimi MM, Vaulay M-J. Colloid Polym Sci 2004;282:314.
[19] Armes SP, Vincent B. J Chem Soc Chem Commun 1987;288.
[20] Cawdery N, Obey TM, Vincent B. J Chem Soc Chem Commun 1988;1189.
[21] Carter FL, editor. Molecular electronic devices. New York: M. Dekker; 1982.
[22] Pich A, Lu Y, Adler HJ, Schmidt T, Arndt KF. Polymer 2002;43:5723.
[23] Boyko V, Pich A, Lu Y, Richter S, Arndt K-F, Adler H-J. Polymer 2003;44:7821.
[24] Pich A, Lu Y, Boyko V, Arndt K-F, Adler H-J. Polymer 2003;44:7651.
[25] Khan MA, Armes SP. Adv Mater 2000;12:671.
[26] Cairns DB, Armes SP. Langmuir 1999;15:8052.
[27] Pich A, Lu Y, Adler H-JP. Colloid Polym Sci 2003;281:907.
[28] Smits FM. Bell Syst Tech J 1958;37:371.
[29] Wu C. Macromolecules 1994;27:7099.
[30] Wu C. Macromolecules 1994;27:298.
[31] Wu C, Akashi M, Chen M-Q. Macromolecules 1997;30:2187.
[32] Elyasevich GK, Rosova EYu, Sidirovich AV, Kuryndin IS, Trchova M, Stejskal J. Eur Polym J 2003;39:647.
[33] Perruchot C, Chehimi MM, Delamar M, Cabet-Deliry E, Miksa B, Slomkovski S, et al. Colloid Polym Sci 2000;278:1139.
[34] Mravčáková M, Boukerma K, Omastová M, Chehimi MM. Mater Sci Eng C 2006;26:306.
[35] Chehimi MM, Abel M-L, Perruchot C, Delamar M, Lascelles SF, Armes SP. Synth Met 1999;104:51.
[36] Omastová M, Pavlinec J, Pionteck J, Simon F, Košina S. Polymer 1998;39:6559.
[37] Maeda S, Corradi R, Armes SP. Macromolecules 1995;28:2905.
[38] Cho G, Fung BM, Glatzhofer DT, Lee J-S, Shul YG. Langmuir 2001;17:456.
[39] Ilangovan G, Chandrasekara Pillai P. J Solid State Electrochem 1999;3:474.
[40] Stejskal J, Trchová M, Fedorová S, Sapurina I, Zemek J. Langmuir 2003;19:3013.
[41] Stejskal J, Spirková M, Riede A, Helmstedt M, Mokreva P, Prokeš J. Polymer 1999;40:2487.
[42] Stejskal J, Spirková M, Kratochvíl P. Acta Polym 1994;45:385.
[43] Stejskal J, Kratochvíl P, Spirková M. Polymer 1995;36:4135.
[44] Sobisch T, Lerche D. Colloid Polym Sci 2000;278:369.
[45] Nešpůrek S, Silinsh EA. Phys Status Solidi A 1976;34:747.
[46] Frank RI, Simmons JG. J Appl Phys 1967;38:832.
[47] Wright GT. Solid-State Electron 1961;2:165.
[48] Godlewski J, Kalinowski J. Phys Status Solidi 1979;56:293.
[49] Bobo JF, Couders S, Arnoult A, Fontaine C, Mamy R. Solid-State Electron 2004;48:845.
[50] Lampert MA, Mark P. Current injection in solids. New York: Academic Press; 1970.
[51] Geng W, Li N, Li X, Wang R, Tu J, Zhang T. Sens Actuators B 2007;125:114.
[52] Kulwicki BM. J Phys Chem Solids 1984;45:1015.